





RESEARCH ARTICLE | SEPTEMBER 18 2023


## New explicit formula for inertial lift in confined flows

Jinghong Su ; Xu Zheng ; Guoqing Hu  



*Physics of Fluids* 35, 092010 (2023)


<https://doi.org/10.1063/5.0168474>



### Physics of Fluids

Special Topic: K. R. Sreenivasan:  
A Tribute on the occasion of his 75th Birthday

**Submit Today**



# New explicit formula for inertial lift in confined flows

Cite as: Phys. Fluids **35**, 092010 (2023); doi: [10.1063/5.0168474](https://doi.org/10.1063/5.0168474)

Submitted: 19 July 2023 · Accepted: 31 August 2023 ·

Published Online: 18 September 2023






View Online



Export Citation



CrossMark

Jinghong Su,<sup>1,2</sup>  Xu Zheng,<sup>3</sup>  and Guoqing Hu<sup>1,a)</sup> 

## AFFILIATIONS

<sup>1</sup>Department of Engineering Mechanics, State Key Laboratory of Fluid Power and Mechatronic Systems, Zhejiang University, Hangzhou 310027, China

<sup>2</sup>Center for Combustion Energy, Key Laboratory for Thermal Science and Power Engineering of Ministry of Education, Department of Energy and Power Engineering, Tsinghua University, Beijing 100084, China

<sup>3</sup>The State Key Laboratory of Nonlinear Mechanics (LNM), Institute of Mechanics, Chinese Academy of Sciences, Beijing 100190, China

<sup>a)</sup>Author to whom correspondence should be addressed: [ghu@zju.edu.cn](mailto:ghu@zju.edu.cn)

## ABSTRACT

Inertial migration has proven effective for high-throughput manipulation of tiny particles in confined flows. However, complex and even controversial relationships between hydrodynamic forces and flow conditions hinder the development of an explicit formula for inertial lift acting on finite-sized particles at Reynolds numbers in the hundreds. Herein, we reveal the different scaling laws for shear gradient-induced inertial lift and wall-induced inertial lift by separating the contributions of pressure stress and viscous stress. A direct result of this treatment is a new explicit formula for the total inertial lift, valid for Reynolds numbers up to 400 and particle blockage ratios up to 0.25. This study provides an alternative way to understand inertial lift, thereby greatly facilitating the prediction of particle migration in practical microfluidic applications.

Published under an exclusive license by AIP Publishing. <https://doi.org/10.1063/5.0168474>

## I. INTRODUCTION

Inertial migration was first observed in a cylindrical pipe, where neutrally buoyant spheres migrate along streamlines to an annulus with a radius of  $\sim 0.6$  times the pipe radius.<sup>1–3</sup> This counterintuitive phenomenon is called the tubular pinch effect and has attracted much interest in explaining its mechanism. For cross-stream migration to occur, the inertial contribution to the flow governed by the Navier–Stokes equations must be significant.<sup>4</sup> However, such a nonlinear inertial term introduces great complexity into the Navier–Stokes equations and limits theoretical analysis to simplified model systems (e.g., flow between parallel plates) with the particle blockage ratio  $a/H \ll 1$ , where  $a$  is the particle size and  $H$  is the channel height.<sup>5–9</sup> Over the past two decades, the development of inertial microfluidics has revived interest in the study of inertial migration, particularly for inertial migration of finite-sized particles in confined flows.<sup>10–17</sup> Since Di Carlo *et al.*<sup>11</sup> performed the first experiment using inertial effect to focus and separate microparticles and cells in curved microchannels, many works have demonstrated the advantages of inertial effect for high throughput manipulation of various particles in microfluidic platforms.<sup>18–22</sup>

The inertial migration of microparticles is mainly determined by the shear gradient-induced lift force and the wall-induced lift force, which are generally summed and referred to as inertial lift.<sup>6</sup> Square or rectangular channels are the most commonly used structures in microfluidic applications.<sup>18</sup> In these situations, finite-sized particles initially migrate rapidly into square or rectangular annuli and then slowly concentrate into stable equilibrium positions within the annuli near the wall centers and channel corners.<sup>13</sup> There can be two, four, or eight equilibrium positions depending on the particle blockage ratio, channel width/height ratio, and Reynolds number.<sup>10,14,19</sup> To predict the migration trajectories and equilibrium positions, our group proposed a method<sup>23</sup> to correct Ho and Leal's lift formula<sup>6</sup> by considering the slip-shear lift and the correction of the shear gradient-induced lift. Later, we provided a new alternative approach based on machine learning<sup>24</sup> to obtain the inertial lift.

To date, many attempts have been made to derive the inertial lift formula for finite-sized particles.<sup>23,25–27</sup> Ho and Leal<sup>6</sup> were the first to theoretically propose an explicit formula for the inertial lift  $F_L$  in a plane Poiseuille flow, i.e.,  $F_L = C_L \rho U_m^2 a^4 / H^2$ , where  $C_L$  is the lift coefficient,  $\rho$  is the fluid density, and  $U_m$  is the maximum fluid velocity.

However, the  $a/H \ll 1$  constraint precludes direct application to microfluidics, where the particle size is often comparable to the channel size. Numerical simulations have also been used to study inertial lift. Di Carlo *et al.*<sup>12</sup> numerically studied inertial lift in a square channel and found  $F_L = C_L \rho U_m^2 a^3 / H$  near the channel center and  $F_L = C_L \rho U_m^2 a^6 / H^4$  near the channel wall, and confirmed that this scaling law is valid for  $a/H > 0.1$ . Based on the above results, Hood, Lee, and Roper<sup>26</sup> emphasized that an  $O(a^5)$  correction term should be included to extend the scaling law of Ho and Leal<sup>6</sup> for finite-sized particles. Recently, Asmolov *et al.*<sup>27</sup> proposed a formula for finite-sized particles at Reynolds number  $Re \leq 20$  ( $Re = \rho U_m H / \mu$ , where  $\mu$  is the fluid viscosity) in the form  $F_L = [c_1 + c_2(a/H)^{-1} + c_3(a/H)^{-2}] \rho U_m^2 a^4 / H^2$ , where  $c_1$ ,  $c_2$ , and  $c_3$  are lift coefficients. The existing results manifest different scaling dependencies of the dimensionless force  $F_L / (\rho U_m^2 a^2)$  on the dimensionless quantity  $a/H$ , indicating that the physical contribution to the inertial lift force has been a controversial issue. Such inconsistency suggests an urgent need to clarify the role of critical parameters, including the Re number and the particle blockage ratio, in the precise formulation of inertial lift. The inertial lift  $F_L$  has typically been obtained by integrating and summing the pressure and viscous stresses acting on the particle surface.<sup>12,19,28</sup> In other words, the inertial lift consists of a pressure-induced inertial lift (hereafter referred to as pressure lift,  $F_{LP}$ ) and a viscosity-induced inertial lift (hereafter referred to as viscous lift,  $F_{LV}$ ), i.e.,  $F_L = F_{LP} + F_{LV}$ . To the best of our knowledge, all existing studies have treated  $F_L$  as a whole by integrating the total stresses. In contrast, in this work, we characterize  $F_{LP}$  and  $F_{LV}$  separately and reveal the different scaling laws under different conditions. We aim to clarify how the shear gradient effect and the wall effect affect the lift force and propose a new explicit formula for  $F_L$  based on particle size, Re number, and particle lateral position.

II. METHODOLOGY

Particles suspended in the flow field are subject to pressure stress from the pressure field and viscous stress from the velocity field. These two stresses make up the total hydrodynamic force acting on the particles. We perform three-dimensional direct numerical simulations (DNS) to evaluate the contributions of the pressure and viscous stresses (see Fig. 1). The channel center is set as the origin of the coordinates, and the  $x$ -axis,  $y$ -axis, and  $z$ -axis are the channel length,

height, and width directions, respectively. A fully developed Poiseuille flow velocity profile for the channel cross section is imposed at the inlet, and the flow is in the  $x$ -axis direction. The pressure constraint of  $p + \partial p / \partial n = 0$  is imposed at the outlet. The no-slip boundary conditions are applied to the channel walls and the particle surface. To accurately predict the interaction between the particle surface and surrounding flow, the Navier–Stokes equations for incompressible flow and Newton’s second law for particle motion are numerically coupled on the structured overlapping grids using the object-oriented framework Overture.<sup>29</sup> The Navier–Stokes equations are

$$\nabla \cdot \mathbf{u} = 0, \tag{1}$$

$$\frac{\partial \mathbf{u}}{\partial t} + \mathbf{u} \cdot \nabla \mathbf{u} = -\frac{\nabla p}{\rho} + \frac{\mu}{\rho} \nabla^2 \mathbf{u}, \tag{2}$$

where  $\mathbf{u}$  is the fluid velocity vector,  $t$  is the time, and  $p$  is the pressure. The equations for particle motion are

$$m_p \frac{d\mathbf{U}}{dt} = \int_{\Sigma} (-p\mathbf{1} + \boldsymbol{\tau}) \cdot \mathbf{n} d\sigma, \tag{3}$$

$$\frac{d(\mathbf{I} \cdot \boldsymbol{\omega})}{dt} = \int_{\Sigma} (\mathbf{x} - \mathbf{x}_c) \times [(-p\mathbf{1} + \boldsymbol{\tau}) \cdot \mathbf{n}] d\sigma, \tag{4}$$

where  $m_p$  is the particle mass,  $\mathbf{U}$  is the velocity of the particle centroid,  $\mathbf{1}$  is the unit tensor,  $\boldsymbol{\tau}$  is the shear rate tensor with  $\tau_{ij} = \mu(\partial u_i / \partial x_j + \partial u_j / \partial x_i)$ ,  $\mathbf{n}$  is the unit normal vector of the particle surface,  $\mathbf{I}$  is the moment of inertia tensor of the particle,  $\boldsymbol{\omega}$  is the angular velocity vector,  $\mathbf{x}_c$  is the position of the particle centroid, and the particle surface is denoted by  $\Sigma$ . To obtain the lift forces at a given lateral position, the particles are constrained to translate only in the  $x$ -axis direction but are free to rotate. Once the translational and rotational motions have both reached steady states, the forces  $F_{LP}$ ,  $F_{LV}$ , and  $F_L$  are calculated by integrating the pressure stress, viscous stress, and total stress on the particle surface, respectively, i.e.,

$$F_{LP} = \int_{\Sigma} -p n d\sigma, \tag{5}$$

$$F_{LV} = \int_{\Sigma} \boldsymbol{\tau} \cdot \mathbf{n} d\sigma, \tag{6}$$

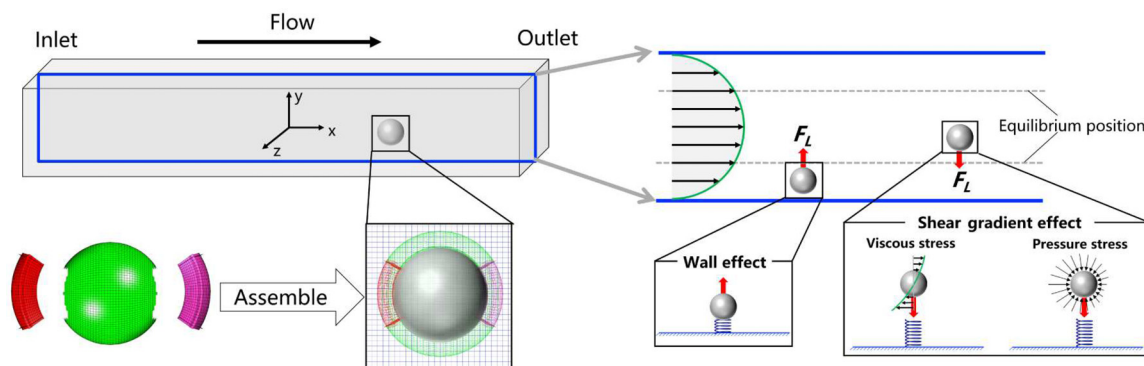


FIG. 1. The schematics of the system. The overlapping grid for a sphere in a square microchannel consists of four component grids: the Cartesian grid for the channel (in blue), the body-fitted grid for the sphere (in green), and two additional grids for the poles of the sphere (in red and purple). In this work, we examine the pressure lift and the viscous lift separately to reveal the scaling dependence of the dimensionless inertial lift and the dimensionless particle size.

$$F_L = \int_{\Sigma} (-p\mathbf{1} + \boldsymbol{\tau}) \cdot \mathbf{n} d\sigma. \quad (7)$$

The details of the simulation process can be found in our previous works.<sup>19,24,30</sup> The inertial lift coefficient  $C_L = F_L/(\rho U_m^2 a^4/H^2)$  is used to characterize the dimensionless inertial lift.<sup>6,9</sup> Similarly,  $C_{LP} = F_{LP}/(\rho U_m^2 a^4/H^2)$  and  $C_{LV} = F_{LV}/(\rho U_m^2 a^4/H^2)$  are the dimensionless pressure lift and the dimensionless viscous lift, respectively.

### III. RESULTS

Figure 2 shows the lift forces for three different sizes  $a/H = 0.10$ ,  $0.20$ , and  $0.30$ . Due to geometric symmetry, only a quarter of the channel cross section is plotted in Figs. 2(a)–2(c). The pressure lift  $C_{LP}$  tends to concentrate particles near the center of the channel wall for all  $a/H$  [see Fig. 2(a)]. In contrast, the viscous lift  $C_{LV}$  tends to concentrate particles near the center of the channel wall (indicated by the solid circle) for  $a/H = 0.10$ , induces unstable particle migration near the channel corner (indicated by the dashed ellipse) for  $a/H = 0.20$ , and concentrates particles near the channel corner (indicated by the solid circle) for  $a/H = 0.30$  [see Fig. 2(b)]. The total lift force, as the sum of  $C_{LP}$  and  $C_{LV}$ , results in particle focusing near the center of the channel wall for all  $a/H$ , and leads to unstable particle migration

near the channel corner for  $a/H = 0.30$  [see Fig. 2(c)]. During migration, particles near the channel center or wall are pushed toward a square annulus by the combined action of  $C_{LP}$  and  $C_{LV}$ , as shown by the red regions in Fig. 2(c), which represent the positions of zero net lift force. The position of the square annulus, quantified by  $y/H$ , decreases with increasing  $a/H$ . Since the square annuli of the two lift forces do not coincide, we call the overlapping region between two square annuli of  $C_{LP}$  and  $C_{LV}$  the competition region. We compute the variations of three types of lift forces along  $y/H$  for different  $a/H$ , as shown in Figs. 2(d)–2(f). Within the competition region [vertical shadow bands in Figs. 2(d)–2(f)], the pressure lift  $C_{LP}$  points toward the channel wall, while the viscous lift  $C_{LV}$  points toward the channel center. Note that the positive lift is defined as pointing toward the channel wall. The particles reach the final focusing position when the two types of lift forces are in equilibrium.

In Figs. 2(a) and 2(b), the pressure lift  $C_{LP}$  shows similar contours for different values of  $a/H$  while the viscous lift  $C_{LV}$  obviously decreases with increasing  $a/H$ , indicating that  $C_{LP}$  is not sensitive to  $a/H$  but  $C_{LV}$  is strongly related to  $a/H$ . The independence between  $C_{LP}$  and  $a/H$  in the near-center region ( $y/H < 0.2$ ) of the channel is also demonstrated in Fig. 3(a), where the data of  $C_{LP}$  for different  $a/H$  collapse into a single line. Furthermore, since the best fit exponent  $n$  for

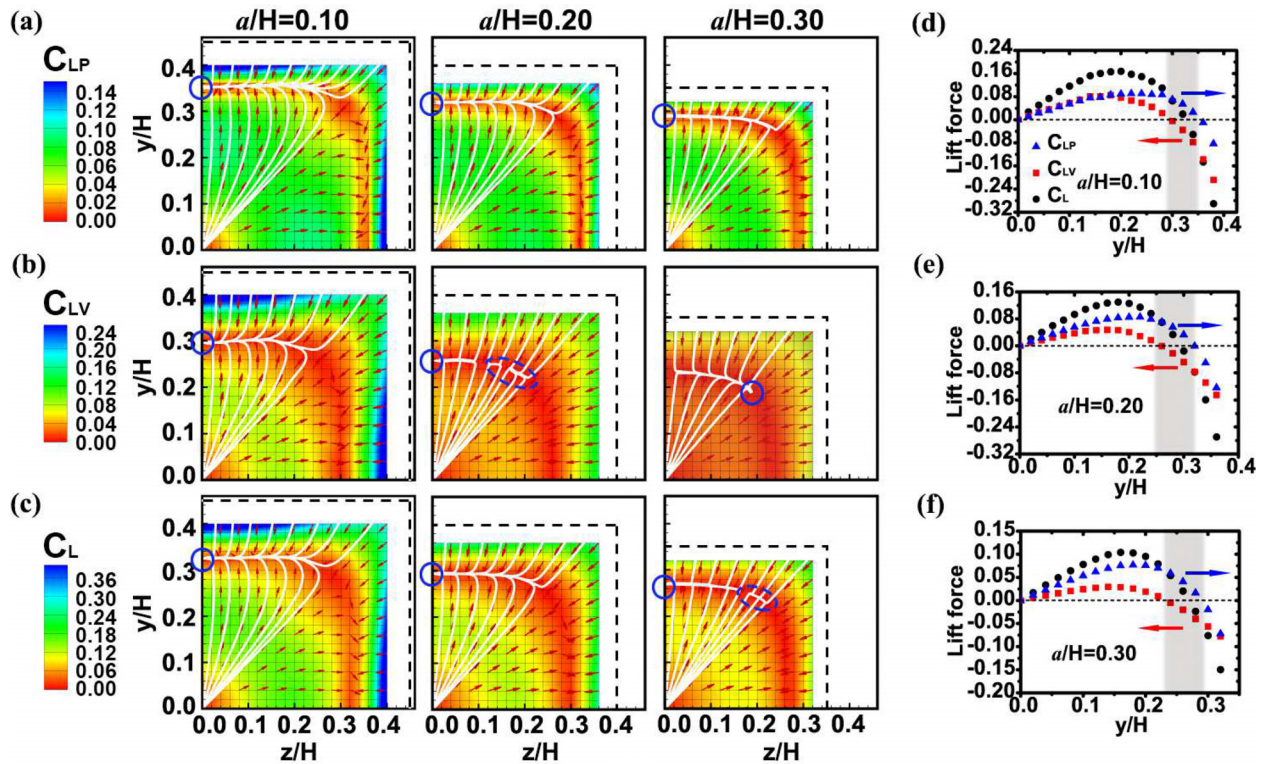


**FIG. 2.** Lift forces in a channel with a square cross section for  $Re = 100$ . The  $C_{LP}$  (a),  $C_{LV}$  (b), and  $C_L$  (c) are shown in a quarter section with the channel center at  $(y/H, z/H)$  of  $(0.0, 0.0)$ . These three types of lift forces are plotted with vectors for directions and contours for magnitudes. The grid is drawn with the grid points corresponding to the particle centers. The black dashed lines mark the outermost position of the particle center, i.e., particles cannot move into the area beyond these lines. The migration trend is marked by the white solid lines. The solid circles denote the stable equilibrium positions and the dashed ellipses denote the unstable equilibrium positions. To avoid masking the contours, the migration trend and equilibrium positions are marked only in half of the plotted region, where the lift forces are symmetrical to those in the other half. The three types of lift forces along the  $y$ -axis are compared for  $a/H = 0.10$  (d),  $a/H = 0.20$  (e) and  $a/H = 0.30$  (f). The blue and red arrows in (d)–(f) indicate the direction of  $C_{LP}$  and  $C_{LV}$ , respectively, within the competition regions (vertical shadow bands).



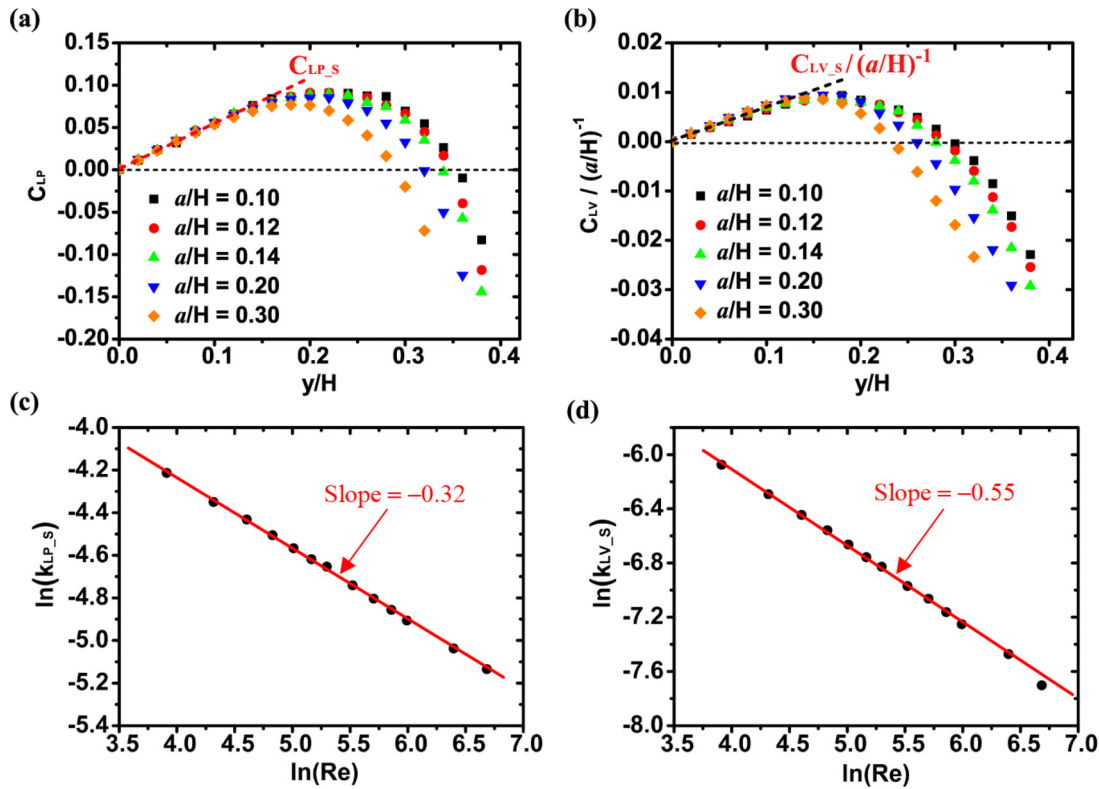


**FIG. 3.** Investigation of the lift forces near the channel center. The data of  $C_{LP}$  (a) and  $C_{LV}/(a/H)^{-1}$  (b) for different  $a/H$  collapse into a single line near the channel center, which is marked by  $C_{LP,S}$  (red dashed lines) and  $C_{LV,S}/(a/H)^{-1}$  (black dashed lines), respectively.  $k_{LP,S}$  (c) and  $k_{LV,S}$  (d) are linearly related to  $Re$  in logarithmic coordinates. The black dots and red lines denote the calculated and fitted data, respectively.

$C_{LV} \sim (a/H)^n$  is close to  $-1$  in the near-center region (see Fig. 4), we compute  $C_{LV}/(a/H)^{-1}$  for different  $a/H$  [see Fig. 3(b)]. The data of  $C_{LV}/(a/H)^{-1}$  collapse into a single line in the near-center region, demonstrating the scaling of  $C_{LV} \sim (a/H)^{-1}$ . Outside the near-center region ( $y/H > 0.2$ ), where the wall effect kicks in, both  $C_{LP}$  and  $C_{LV}/(a/H)^{-1}$  deviate from the scaling laws observed in the near-center region, indicating that the wall effect has a different dependence on  $a/H$ .

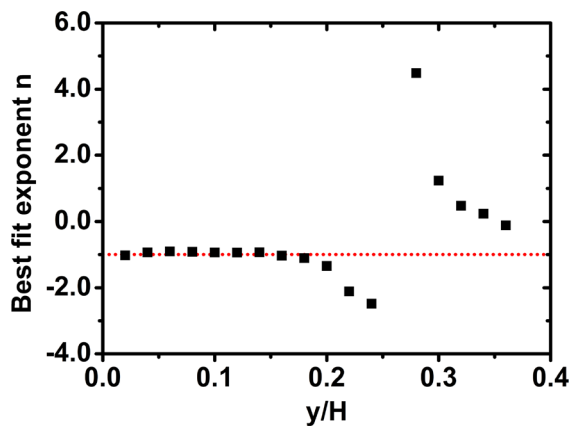


**FIG. 4.** The best fit exponent  $n$  for  $C_{LV} \sim (a/H)^n$  under  $Re = 100$ .

To distinguish between the shear gradient effect and the wall effect, we introduce the shear gradient-induced pressure lift ( $C_{LP,S}$ ) and the shear gradient-induced viscous lift ( $C_{LV,S}$ ) as two components of the shear gradient-induced inertial lift ( $C_{L,S}$ ), i.e.,  $C_{L,S} = C_{LP,S} + C_{LV,S}$ . The wall-induced pressure lift  $C_{LP,W} = C_{LP} - C_{LP,S}$ , the viscous lift  $C_{LV,W} = C_{LV} - C_{LV,S}$ , and the inertial lift  $C_{L,W} = C_L - C_{L,S}$ , where  $C_{L,W} = C_{LP,W} + C_{LV,W}$ .

Previous theoretical and numerical studies have shown that the inertial lift near the channel center is approximately linearly proportional to  $y$ .<sup>6,8,23</sup> The collapsed lines in Figs. 3(a) and 3(b) within the near-center region can, thus, be characterized by  $C_{LP,S} = k_{LP,S}(y/H)$  and  $C_{LV,S}/(a/H)^{-1} = k_{LV,S}(y/H)$ , where  $k_{LP,S}$  and  $k_{LV,S}$  are the pressure lift and viscous lift coefficients, respectively.  $k_{LP,S}$  and  $k_{LV,S}$  at  $Re$  values from 50 to 800 are plotted in Figs. 3(c) and 3(d), and they decrease linearly with  $Re$  in logarithmic coordinates, indicating that both  $k_{LP,S}$  and  $k_{LV,S}$  are power functions of  $Re$ . The power functions of  $k_{LP,S} = 2.6Re^{-0.32}$  and  $k_{LV,S} = Re^{-0.55}$  are assumed to fit the data from the simulations very well (see Fig. S1). We now obtain an explicit expression for the shear gradient-induced inertial lift, which dominates in the near-center region ( $y/H < 0.2$ ),

$$C_{L,S} = C_{LP,S} + C_{LV,S} = (2.6Re^{-0.32} + Re^{-0.55}(a/H)^{-1})(y/H). \quad (8)$$

We then turn to the wall-induced lift force, which can be obtained by subtracting the shear gradient-induced lift from the total

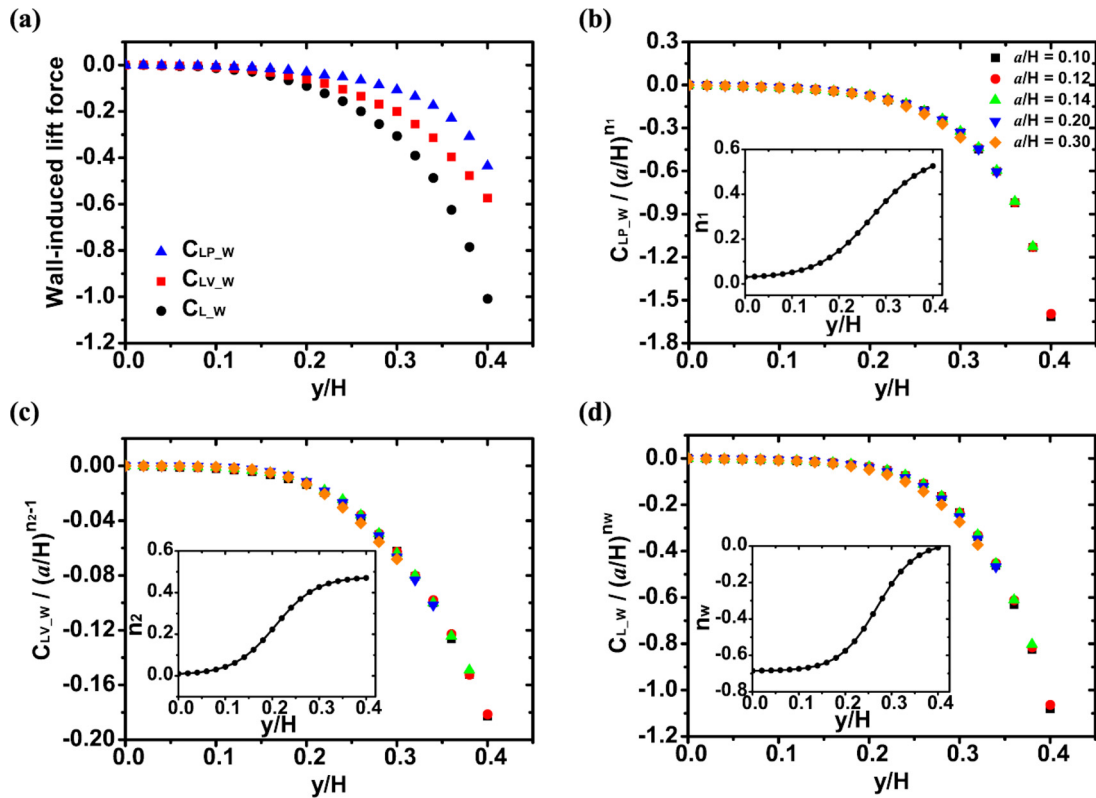


**FIG. 5.** The dependence of the wall-induced lift forces on  $a/H$ . (a) The total wall-induced lift force  $C_{L-W}$  is the sum of the wall-induced pressure lift force  $C_{LP-W}$  and the wall-induced viscous lift force  $C_{LV-W}$ . These three types of wall-induced lift forces for different  $a/H$  can collapse to a single curve through  $C_{LP-W}/(a/H)^{n_1}$  (b),  $C_{LV-W}/(a/H)^{n_2-1}$  (c), and  $C_{L-W}/(a/H)^{n_w}$  (d). The  $n_1$ ,  $n_2$ , and  $n_w$  are S-shaped along the  $y$ -axis and are shown in inset (b), inset (c), and inset (d), respectively.

lift [see Fig. 5(a)]. Similar to the treatment of the shear gradient-induced lift force, we divide the wall-induced lift into a pressure lift  $C_{LP-W}$  and a viscous lift  $C_{LV-W}$ . As shown in Figs. 5(b) and 5(c), the pressure lift  $C_{LP-W}$  and the viscous lift  $C_{LV-W}$  collapse into a single curve by dividing by  $(a/H)^{n_1}$  and  $(a/H)^{n_2-1}$ , respectively. The exponents  $n_1$  and  $n_2 - 1$  quantify the dependence of the pressure part and the viscous part of the wall-induced lift on the particle size, i.e.,  $C_{LP-W} \sim (a/H)^{n_1}$  and  $C_{LV-W} \sim (a/H)^{n_2-1}$ . In particular, since the pressure part and the viscous part of the shear gradient-induced lift obey  $C_{LP-S} \sim (a/H)^0$  and  $C_{LV-S} \sim (a/H)^{-1}$ , the exponents  $n_1$  and  $n_2$  characterize the difference between the dependence induced by the wall effect and the shear gradient effect. We found that  $n_1 \approx 0$  and  $n_2 \approx 0$  near the channel center and  $n_1 \approx 0.5$  and  $n_2 \approx 0.5$  near the channel wall, manifesting an S-shaped variation along the  $y$ -axis [insets in Figs. 5(b)–5(c)]. The S-shaped variation shows that both  $n_1$  and  $n_2$  increase with  $y/H$ , indicating that the difference increases with distance from the channel center. In addition, a similar function,  $C_{L-W}/(a/H)^{n_w}$ , can collapse all the data of the wall-induced lift  $C_{L-W}$  into a single curve [see Fig. 5(d)]. Here, the exponent  $n_w$  also has an S-shaped distribution.

We found that decomposing the wall-induced inertial lift into pressure and viscous components did not simplify the problem but rather made the formula more complicated. We, therefore, decided to establish the formula for the wall-induced lift  $C_{L-W}$  directly from Fig. 5(d).

The exponent  $n_w$  can be fitted by a sigmoid function,  $n_w = 0.02 - 0.7/(1 + e^{24.34(y/H-0.27)})$  [see the inset in Fig. 5(d)]. The half S-shape of the curve of  $C_{L-W}/(a/H)^{n_w}$  in Fig. 5(d) inspires us to take another sigmoid function,  $C_{L-W}/(a/H)^{n_w} = -(2.6/(1 + e^{-\alpha(y/H-\beta)}) - \gamma)$ , to mathematically describe the wall-induced lift  $C_{L-W}$ . Thus, we can formulate the wall-induced inertial lift as

$$C_{L-W} = -(2.6/(1 + e^{-\alpha(y/H-\beta)}) - \gamma)(a/H)^{n_w}, \quad (9)$$

where the coefficients of  $\alpha$ ,  $\beta$ , and  $\gamma$  depend only on the Re number and satisfy the relation  $\gamma = 2.6/(1 + e^{\alpha\beta})$  to guarantee  $C_{L-W} = 0$  at the center of the channel. In Figs. 6(a) and 6(b), we study the variation of  $\alpha$  and  $\beta$  with  $y/H$  at Re numbers ranging from 50 to 400. The fitted polynomials are obtained as  $\alpha = 22.73 - 0.033\text{Re} + 2.64 \times 10^{-5}\text{Re}^2$  and  $\beta = 0.373 + 5.1 \times 10^{-4}\text{Re} - 3.4 \times 10^{-7}\text{Re}^2$ .

Based on  $C_L = C_{L-S} + C_{L-W}$ , we obtain the final explicit formula for the total inertial lift

$$C_L = (2.6\text{Re}^{-0.32} + \text{Re}^{-0.55}(a/H)^{-1})(y/H) - (2.6/(1 + e^{-\alpha(y/H-\beta)}) - \gamma)(a/H)^{n_w}. \quad (10)$$

The corresponding MATLAB code is provided in the supplementary material. This formula shows excellent performance in predicting the inertial lifts for Re numbers up to 400 and particle blockage ratios up to  $a/H = 0.25$ , as shown in Figs. 6(c) and 6(d). The inertial lifts

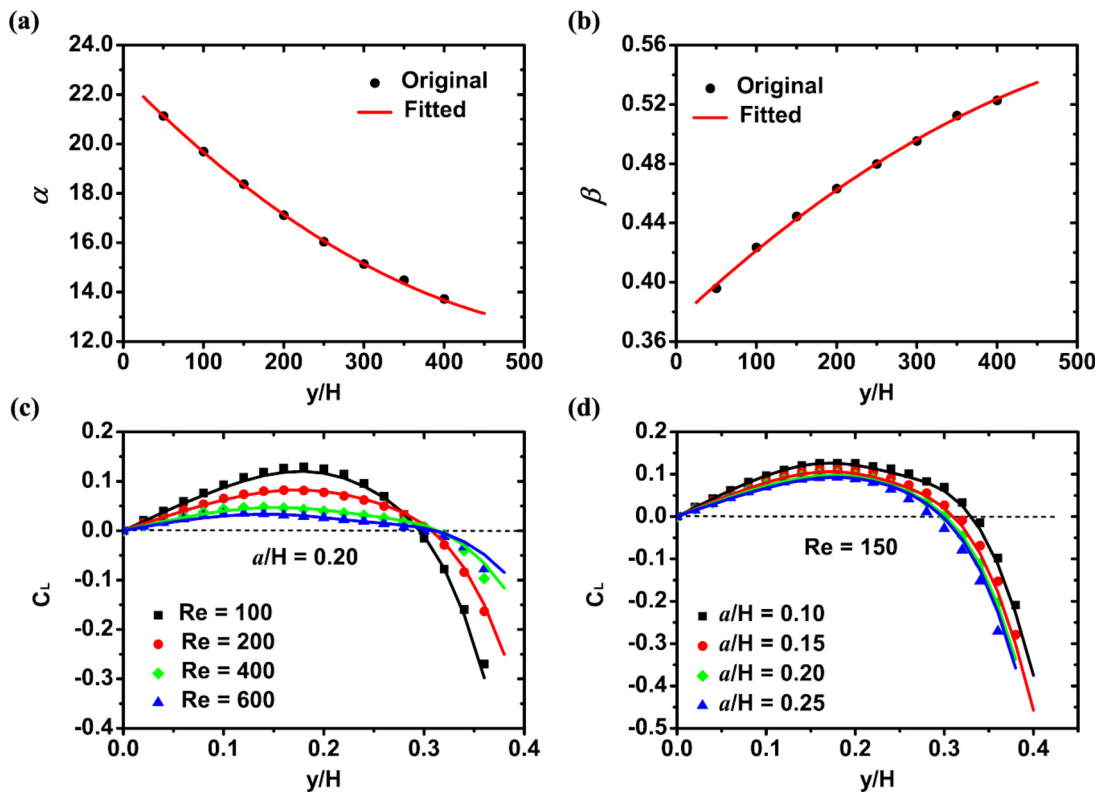


**FIG. 6.** Prediction of the inertial lift force. The coefficients of  $\alpha$  (a) and  $\beta$  (b) are fitted by polynomial functions. The inertial lift is predicted under different Re numbers for a particle of  $a/H = 0.20$  (c) and for particles of different  $a/H$  under  $Re = 150$  (d). The symbols and lines denote the calculated data by DNS and the predicted data in Eq. (10), respectively. The detailed data in (c) and (d) are available in Tables S1–S2 in the supplementary material.

predicted in Eq. (10) are also compared with those from Nakagawa *et al.*,<sup>15</sup> yielding good agreement for  $Re = 80$  and  $a/H = 0.22$  (see Fig. S2 in the supplementary material). In Eq. (10), the influences of particle size, Re number, and lateral position in the channels are completely decoupled, which brings significant convenience in evaluating the inertial lift force for various practical applications.

Furthermore, the present methodology is readily applicable to microchannels with a rectangular cross section. The results for a rectangular microchannel with an aspect ratio (width/height) of 2 at  $Re = 100$  are shown in Fig. 7. Similar to the square channel, the scaling laws obeyed by the pressure part and the viscous part of the shear gradient-induced lift are  $C_{LP,S} \sim (a/H)^0$  and  $C_{LV,S} \sim (a/H)^{-1}$  are also valid when the particles are on the long axis of the rectangular microchannel [see Figs. 7(a) and 7(b)]. In addition, the S-shaped function can also be used to collapse all the data of the wall-induced lift into a single curve [see Fig. 7(c)]. Using the above methodology, we summarize the corresponding formula in Table S3 in the supplementary material. The inertial lift forces obtained by the formula and DNS are in good agreement, as shown in Fig. 7(d).

#### IV. DISCUSSION

This work aims us to explain the controversy about the scaling dependence of the dimensionless inertial lift and the dimensionless particle size. To address this issue, we propose a novel approach to decompose the inertial lift into a pressure-contributing component

and a viscous-contributing component. In doing so, we clarify the reasons for the different scaling dependencies observed in different studies. In particular, we find that the pressure-contributing and viscous-contributing components of the shear gradient-induced inertial lift have different scaling dependencies on particle size, which has hindered the investigation of the scaling dependence of inertial lift on particle size in previous studies. Furthermore, these two components also have different dependencies on the Reynolds number, further complicating related studies. Our work has successfully overcome these obstacles and effectively established the relationship between inertial lift and particle size.

Our work provides a complete and explicit formula for the total inertial lift that can be applied to situations with Re numbers up to 400 and blockage ratio  $a/H$  up to 0.25. We have also investigated the cases for larger Re and  $a/H$  beyond these limits. For Re number slightly beyond 400 (e.g.,  $Re = 600$ ), we found that the explicit formula can effectively capture the inertial lift near the center of the channel, while its prediction performance for the inertial lift near the channel wall is less accurate. The deviation of the data has been observed in Fig. 6(c). For  $Re = 600$ , the deviation of the lift force near the channel wall could be more than 30%. Previous studies have shown that with the increasing of the Re number, the focus position changes from one ring to two rings in a circular tube,<sup>31</sup> indicating a change in the relationship between inertial lift and Re number at high Re number conditions. For particles with larger blockage ratios, the blocking effect of the particles

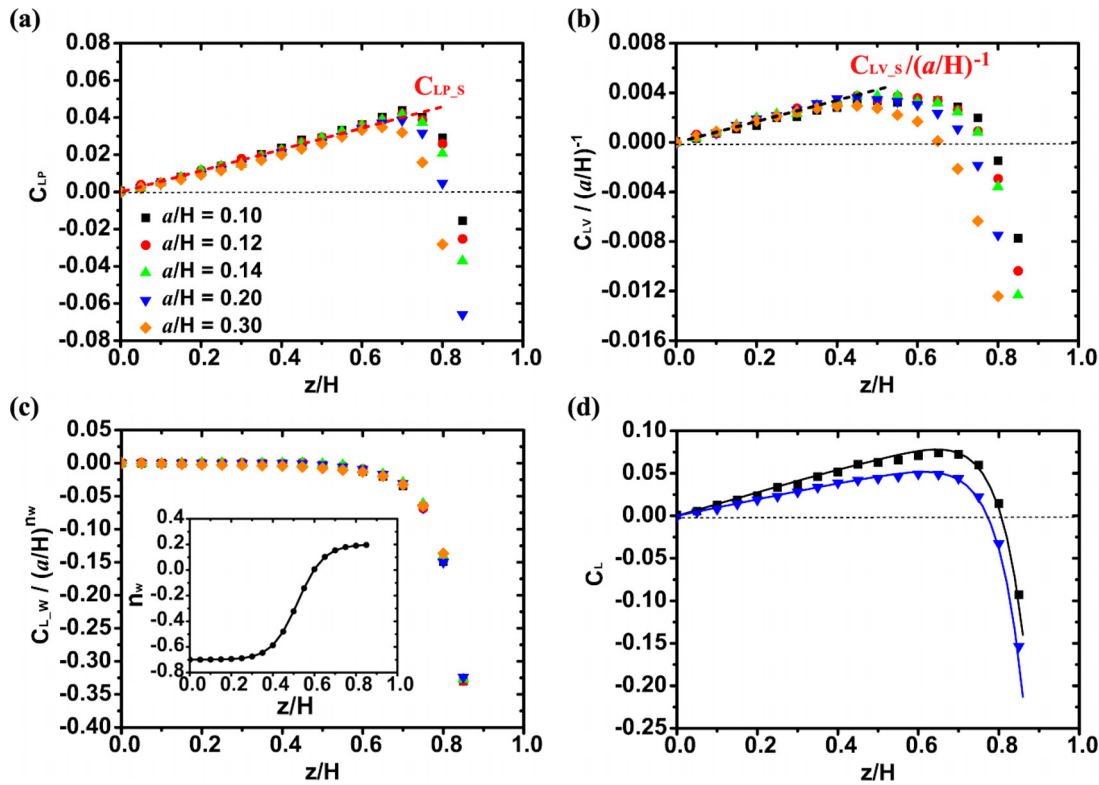


**FIG. 7.** Investigation of the inertial lift for a rectangular channel under  $Re = 100$ . Here, the particles are on the long axis ( $z$ -axis) of the rectangular channel with a width/height ratio of 2. The data of  $C_{LP}$  (a) and  $C_{LV}/(a/H)^{-1}$  (b) for different  $a/H$  collapse to a single line near the channel center, which is marked by  $C_{LP,S}$  (red dashed lines) and  $C_{LV,S}/(a/H)^{-1}$  (black dashed lines), respectively. The wall-induced inertial lift for different  $a/H$  can collapse into a single curve by  $C_{L,W}/(a/H)^{n_w}$  (c). The  $n_w$  is S-shaped along the  $z$ -axis and is shown in the inset (c). (d) The inertial lift forces obtained by the formula in Table S3 (lines) are compared with those obtained by DNS (symbols) under  $a/H = 0.10$  (black) and  $a/H = 0.20$  (blue), showing good agreement.

on the channel flow becomes pronounced. In particular, the wall-induced lift for large particles (e.g.,  $a/H = 0.3$ ) exhibits a noticeable difference compared to that for small particles (e.g.,  $a/H = 0.1$ ). As shown in Fig. 5(d), the wall-induced lift for  $a/H = 0.3$  is nearly 12% less than the collapsed curve near the channel wall, which could make the error of the total inertial lift up to 35%. This error would increase with the blockage ratio.

In our previous work,<sup>24</sup> machine learning was used to obtain the distribution of inertial lift within a rectangular cross section, allowing us to gain insight into the underlying mechanisms. This work clarifies the relationship between shear gradient-induced inertial lift and particle size from different physical sources. In particular, shear gradient-induced pressure lift and viscous lift have different scaling dependencies on particle size as a result of different mechanisms. As the Reynolds number increases, pressure lift gradually becomes dominant, resulting in a higher exponent in its power function with the Reynolds number than in the power function with the Reynolds number for viscous lift. Based on the shear gradient-induced inertial lift, we obtain the explicit expression for the wall-induced inertial lift. In this work, we focus on the inertial lift expression on the principal axis. The inertial lift distribution on the principal axis is highly representative, since the potential equilibrium positions tend to lie on the square or rectangular annuli that pass through the equilibrium positions on the principal axis.

Inertial lift is primarily used to predict the migration behavior and equilibrium positions of particles, especially when other effects (such as viscoelastic, acoustic and magnetic forces) are introduced. Due to the effect of inertial lift, particles tend to migrate to certain locations. When additional forces, such as those mentioned are present, the behavior of particles can become more complex. Our approach using the new formula provides the ability to estimate the magnitude of inertial lift and its relative importance compared to other forces, which is essential for the design and optimization of microfluidic devices.

**V. CONCLUSIONS**

In conclusion, we have studied pressure lift and viscous lift separately in order to gain a deeper understanding of inertial lift. We found that the shear gradient-induced pressure lift and the shear gradient-induced viscous lift obey different scaling laws, i.e., the shear gradient-induced pressure lift scales with the fourth power of the particle diameter, whereas the shear gradient-induced viscous lift scales with the third power of the particle diameter. By subtracting the shear gradient-induced inertial lift from the total inertial lift force, we obtain the wall-induced inertial lift and reveal the position-dependent dependence of the wall-induced inertial lift on particle size. Our work goes beyond existing inertial lift studies and provides a complete and

08 April 2024 03:13:12



explicit formula for the total inertial lift that can be applied over a wide range of  $Re$  (up to 400) and particle blockage ratio  $a/H$  (up to 0.25), as well as different microchannel geometries.

### SUPPLEMENTARY MATERIAL

See the supplementary material for additional information presented in additional figures and data collected in support of Sec. III. The inertial lift forces from DNS and Eq. (10) are compared, and the corresponding MATLAB code for Eq. (10) is provided.

### ACKNOWLEDGMENTS

This work was supported by the Natural Science Foundation of China (Nos. 12272345, 11832017, and 12072350), the Chinese Academy of Sciences Key Research Program of Frontier Sciences (No. QYZDB-SSW-JSC036), the Chinese Academy of Sciences Strategic Priority Research Program (No. XDB22040403), and the National Key R&D Program of China (2022YFF0503504).

### AUTHOR DECLARATIONS

#### Conflict of Interest

The authors have no conflicts to disclose.

#### Author Contributions

Jinghong Su and Xu Zheng contributed equally to this work.

**Jinghong Su:** Conceptualization (equal); Data curation (lead); Formal analysis (lead); Investigation (equal); Methodology (equal); Software (lead); Validation (equal); Visualization (lead); Writing – original draft (equal). **Xu Zheng:** Data curation (equal); Formal analysis (equal); Investigation (equal); Writing – original draft (equal). **Guoqing Hu:** Conceptualization (equal); Funding acquisition (lead); Resources (lead); Supervision (lead); Writing – review & editing (lead).

### DATA AVAILABILITY

The data that support the findings of this study are available from the corresponding author upon reasonable request.

### REFERENCES

- 1G. Segre and A. Silberberg, “Radial particle displacements in poiseuille flow of suspensions,” *Nature* **189**, 209–210 (1961).
- 2G. Segre and A. Silberberg, “Behaviour of macroscopic rigid spheres in poiseuille flow part 1. Determination of local concentration by statistical analysis of particle passages through crossed light beams,” *J. Fluid Mech.* **14**, 115–135 (1962).
- 3G. Segre and A. Silberberg, “Behaviour of macroscopic rigid spheres in poiseuille flow part 2. Experimental results and interpretation,” *J. Fluid Mech.* **14**, 136–157 (1962).
- 4F. Bretherton, “The motion of rigid particles in a shear flow at low reynolds number,” *J. Fluid Mech.* **14**, 284–304 (1962).
- 5S. Rubinow and J. Keller, “The transverse force on a spinning sphere moving in a viscous fluid,” *J. Fluid Mech.* **11**, 447–459 (1961).
- 6B. Ho and L. Leal, “Inertial migration of rigid spheres in two-dimensional unidirectional flows,” *J. Fluid Mech.* **65**, 365–400 (1974).
- 7P. Vasseur and R. Cox, “The lateral migration of a spherical particle in two-dimensional shear flows,” *J. Fluid Mech.* **78**, 385–413 (1976).
- 8J. Schonberg and E. Hinch, “Inertial migration of a sphere in poiseuille flow,” *J. Fluid Mech.* **203**, 517–524 (1989).
- 9E. Asmolov, “The inertial lift on a spherical particle in a plane poiseuille flow at large channel reynolds number,” *J. Fluid Mech.* **381**, 63–87 (1999).
- 10B. Chun and A. J. C. Ladd, “Inertial migration of neutrally buoyant particles in a square duct: An investigation of multiple equilibrium positions,” *Phys. Fluids* **18**, 031704 (2006).
- 11D. Di Carlo, D. Irimia, R. Tompkins, and M. Toner, “Continuous inertial focusing, ordering, and separation of particles in microchannels,” *Proc. Natl. Acad. Sci. U. S. A.* **104**, 18892–18897 (2007).
- 12D. Di Carlo, J. Edd, K. Humphry, H. Stone, and M. Toner, “Particle segregation and dynamics in confined flows,” *Phys. Rev. Lett.* **102**, 094503 (2009).
- 13J. Zhou and I. Papautsky, “Fundamentals of inertial focusing in microchannels,” *Lab Chip* **13**, 1121–1132 (2013).
- 14K. Miura, T. Itano, and M. Sugihara-Seki, “Inertial migration of neutrally buoyant spheres in a pressure-driven flow through square channels,” *J. Fluid Mech.* **749**, 320–330 (2014).
- 15N. Nakagawa, T. Yabu, R. Otomo, A. Kase, M. Makino, T. Itano, and M. Sugihara-Seki, “Inertial migration of a spherical particle in laminar square channel flows from low to high reynolds numbers,” *J. Fluid Mech.* **779**, 776–793 (2015).
- 16I. Lashgari, M. Ardekani, I. Banerjee, A. Russom, and L. Brandt, “Inertial migration of spherical and oblate particles in straight ducts,” *J. Fluid Mech.* **819**, 540–561 (2017).
- 17S. Nakayama, H. Yamashita, T. Yabu, T. Itano, and M. Sugihara-Seki, “Three regimes of inertial focusing for spherical particles suspended in circular tube flows,” *J. Fluid Mech.* **871**, 952–969 (2019).
- 18J. Martel and M. Toner, “Inertial focusing in microfluidics,” *Annu. Rev. Biomed. Eng.* **16**, 371–396 (2014).
- 19C. Liu, G. Hu, X. Jiang, and J. Sun, “Inertial focusing of spherical particles in rectangular microchannels over a wide range of reynolds numbers,” *Lab Chip* **15**, 1168–1177 (2015).
- 20J. Xie and G.-H. Hu, “Computational modelling of membrane gating in capsule translocation through microchannel with variable section,” *Microfluid. Nanofluid.* **25**, 1–16 (2021).
- 21X. Lu and X. Xuan, “Inertia-enhanced pinched flow fractionation,” *Anal. Chem.* **87**, 4560–4565 (2015).
- 22J. Zhang, S. Yan, D. Yuan, G. Alici, N. Nguyen, M. Warkiani, and W. Li, “Fundamentals and applications of inertial microfluidics: A review,” *Lab Chip* **16**, 10–34 (2016).
- 23C. Liu, C. Xue, J. Sun, and G. Hu, “A generalized formula for inertial lift on a sphere in microchannels,” *Lab Chip* **16**, 884–892 (2016).
- 24J. Su, X. Chen, Y. Zhu, and G. Hu, “Machine learning assisted fast prediction of inertial lift in microchannels,” *Lab Chip* **21**, 2544–2556 (2021).
- 25B. Yang, J. Wang, D. Joseph, H. Hu, T. Pan, and R. Glowinski, “Migration of a sphere in tube flow,” *J. Fluid Mech.* **540**, 109–131 (2005).
- 26K. Hood, S. Lee, and M. Roper, “Inertial migration of a rigid sphere in three-dimensional poiseuille flow,” *J. Fluid Mech.* **765**, 452–479 (2015).
- 27E. Asmolov, A. Dubov, T. Nizkaya, J. Harting, and O. Vinogradova, “Inertial focusing of finite-size particles in microchannels,” *J. Fluid Mech.* **840**, 613–630 (2018).
- 28S. R. Bazaz, A. Mashhadian, A. Ehsani, S. C. Saha, T. Krüger, and M. E. Warkiani, “Computational inertial microfluidics: A review,” *Lab Chip* **20**, 1023–1048 (2020).
- 29D. L. Brown, W. D. Henshaw, and D. J. Quinlan, “Overture: An object-oriented framework for solving partial differential equations,” in *International Conference on Computing in Object-Oriented Parallel Environments* (Springer, Berlin, Heidelberg, 1997), pp. 177–184.
- 30J. Su, X. Chen, and G. Hu, “Inertial migrations of cylindrical particles in rectangular microchannels: Variations of equilibrium positions and equivalent diameters,” *Phys. Fluids* **30**, 032007 (2018).
- 31Y. Morita, T. Itano, and M. Sugihara-Seki, “Equilibrium radial positions of neutrally buoyant spherical particles over the circular cross-section in poiseuille flow,” *J. Fluid Mech.* **813**, 750–767 (2017).